AIAA JOURNAL
Vol. 37, No. 11, November 1999

Numerical Simulation of Dynamic Stall Using an Improved Advection Upwind Splitting Method

Yang-Yao Niu*
Chung-Hua University, Hsin-Chu 30067, Taiwan, Republic of China
and
Meng-Sing Liou†
NASA John H. Glenn Research Center at Lewis Field, Cleveland, Ohio 44135

In this study a dual-time integration method with the advection upwind splitting method based on flux difference (AUSMD) scheme is demonstrated with simplicity, robustness, and accuracy in solving the time-dependent full Navier–Stoke equations for aerodynamic analysis of stationary and oscillating airfoils. A pseudotime is introduced as an iteration strategy so that time accuracy for solving the unsteady equations can be preserved for long time. A second-order, time-accurate, Euler backward implicit discretization is made at the physical time level. A two-stage Runge–Kutta scheme is used in the pseudotime iteration, in combination with acceleration enhancement procedures, the local time stepping, and residual smoothing. The recent AUSMD flux scheme with a slight modification is applied for approximating the inviscid terms. This modification has been found necessary to provide robust and accurate solutions for the study of dynamic stall. Meanwhile, the renormalization group theory model is chosen to evaluate the turbulence eddy viscosity. Both light and deep dynamic stall cases were calculated, along with grid refinement and time-stepping size studies. Results of unsteady airload hysteresis curves and instantaneous flow pictures are analyzed and compared with measured data.

Introduction

UNSTEADY stall phenomena are the result of airfoils and wings oscillating in pitch with a maximum angle of attack greater than the static-stall angle. This delay of stall, often accompanied with hysteresis in lift and moment coefficients, has challenged aerodynamicists for many years to find its causes. The dynamic stall appears in such aeronautical problems as flows over helicopter rotor blades and rapid maneuvering aircraft and turbomachines and even during insects' flight. As noted by Carr,[1] Harris and Pruyn[2] studied the aerodynamic characteristics for a helicopter rotor and observed that the extra lift on the helicopter rotor was obtained when the blade moved opposite to the direction of flight. Ham and Garelick[3] found that the increased lift was achieved by oscillating airfoils. In Ham's experiments[4] the hysteresis in lift and drag was believed to result from the vortex shedding on the surface of the airfoils. Carta[5] and Liiva and Davenport[6] observed the dynamic correlation between the pressure distributions on the oscillating airfoil surface and the passage of the vortex over the airfoil. Dynamic stall on a rotor blade was explored by McCroskey and Fisher[7] in an experimental investigation of a model rotor. The dynamic effects were found to be closely associated with the motion of vortex. More information was gathered in the subsequent experiments by this group of researchers (see, for example, Refs. 1 and 8–12).

With the advent of high-performance computers, performing numerical simulations of the dynamic stall problem has become possible. A popular test problem is a dynamic-stall process associated with the NACA standard airfoil oscillating in pitch motion at low reduced frequency and high Reynolds number, as in the previous studies.[13–21] Among these past dynamic-stall simulations, central differencing discretization is most widely employed, but is only partially successful in predicting the dynamic stall, especially for the case of the deep stall. The upwind schemes have been shown in many situations to be superior to the central scheme and hence are the choice of scheme at the outset of this study, with an aim at gaining insight as to the causes for the discrepancies between the numerical solutions and measurements. The Roe scheme, perhaps the most popular upwind scheme today, however, is known to violate entropy conditions, requiring a fix with adjustable problem-dependent coefficients. More seriously, the scheme gives rise to negative density even as flow encounters a relatively moderate expansion, which is an inevitable aspect as the airfoil pitches up and down. A recent hybrid flux splitting, the AUSM family by Liou and Steffen[22] and Liou,[23] has incorporated the accuracy of the flux-difference splitting as well as the efficiency and robustness of the flux-vector splitting and has been found to be free from the preceding deficiencies. In the AUSM schemes the convective part of inviscid fluxes and pressure at the cell interface are represented by polynomial functions, and the passive scalar quantities are convected in the flow direction based on the sense of the interface velocity. The AUSM+ (Ref. 23) is a further improvement of AUSM (Ref. 22), possessing the following features: accurate resolution of stationary and moving shock and contact discontinuities, and positivity preserving of pressure and density.[24] Another variant, termed AUSMD, has been developed by Wada and Liou[25] to achieve the same purposes. Although the family of AUSM schemes has been shown to yield reliable results for various applications, especially for moderate- to high-speed flows, their applications to the low-speed, steady and transient flow problems have not been extensively explored yet. To our knowledge, utilization of the family of AUSM schemes to the dynamic stall problem has not been performed previously.

In this study we evaluate the performance of the AUSMD scheme for the steady-state and oscillating low-speed airfoil flows with high angles of attack. In addition, the renormalization group theory (RNG)-based algebraic model is used to account for the effect of the turbulence. Scrinivasan et al.,[21] in their evaluation of turbulence models for calculating dynamic stall, found that the RNG model gave a reasonable prediction of the nonequilibrium nature of flow separation and the associated time-lag features, but with less computational cost compared to other nonalgebraic turbulence models. In the current RNG model a damping function[26] is included in the mean dissipation rate of Patel et al.[27] to approximate the near-wall flow behaviors from the viscous sublayer to the log-law region, together with the length scale.[21] We present in this paper numerical results for one light and one deep-stall case of NACA 0012 airfoil and compare them with experimental results.[9] Unsteady airload hysteresis curves and instantaneous flow pictures are discussed, with

---

Received 10 November 1997; revision received 8 March 1999; accepted for publication 8 March 1999.

*Associate Professor, Department of Mechanical Engineering. Member AIAA.

†Senior Scientist. Associate Fellow AIAA.

comparisons to experimental measurements as well as numerical results of different grid and physical time-step sizes.

Governing Equations

The two-dimensional Navier–Stokes equations on moving meshes in nondimensional conservative form are written as

$$\frac{\partial Q}{\partial t}+\frac{\partial F}{\partial x}+\frac{\partial G}{\partial y}=\left(\frac{\partial \boldsymbol{F}_v}{\partial x}+\frac{\partial \boldsymbol{G}_v}{\partial y}\right) \tag{1}$$

where $Q=[\rho, \rho u, \rho v, E]$, $F=[\rho U, \rho u U+p, \rho v U, \rho H U]$, and $G=[\rho V, \rho u V, \rho v V+p, \rho H V]$. The viscous flux vectors $\boldsymbol{F}_v, \boldsymbol{G}_v$ are represented as $\boldsymbol{F}_v=[0, \tau_{xx}, \tau_{xy}, R]$, $\boldsymbol{G}_v=[0, \tau_{xy}, \tau_{yy}, S]$. The variables appearing in these terms are given by

$$U=u-x_t, \qquad V=v-y_t$$

$$R=u\tau_{xx}+v\tau_{xy}+\alpha\frac{1}{Re}\frac{\partial a^2}{\partial x}, \qquad S=u\tau_{xy}+v\tau_{yy}+\alpha\frac{1}{Re}\frac{\partial a^2}{\partial y}$$

$$\alpha=\mu Pr^{-1}(\gamma-1)^{-1}$$

The variables ρ, u, v, p, a, E, and H are the density, the x- and y-velocity components, static pressure, speed of sound, total energy, and total enthalpy, respectively, along with the grid velocity components x_t and y_t. The viscous terms involve stress components τ_{xx}, τ_{xy}, and τ_{yy} and Reynolds and Prandtl numbers Re and Pr. For the turbulent flow simulation the viscosity coefficient μ is divided into the laminar viscosity and the turbulent viscosity. The laminar viscosity is described by the Sutherland law, and the turbulent viscosity is evaluated by the RNG-based algebraic turbulence model, as briefly given in the following.

In the RNG-based algebraic turbulence model there is a length scale L needed to be specified outside the RNG theory. The integral length scale is assumed to be proportional to the boundary-layer thickness δ and is corresponded to the smallest scales retained in the system after the RNG procedure of fluctuating mode eliminations. In terms of the dissipation rate and the integral length scale, the eddy viscosity is expressed in the following formula:

$$\nu=\nu_t+\nu_l=\nu_l\left[1+H\left(\frac{0.0192}{\nu_l^3}\epsilon L^{-4}-C\right)\right]^{\frac{1}{3}} \tag{2}$$

where the subscripts l and t refer to the laminar viscosity and turbulent viscosity, respectively. $C=\mathcal{O}(100)$ is the RNG constant, and H is the Heaviside step function; hence the turbulence viscosity turns on as its argument is positive, namely,

$$\frac{0.0192}{\nu_l^3}\epsilon L^{-4}>C \tag{3}$$

Following the work,[21] the integral length scale is assumed to be proportional to the boundary-layer thickness δ as $\delta=1.2y_{1/2}$, where $y_{1/2}$ is the normal distance from the wall at which the vorticity function attains its half amplitude. The length scale is evaluated as

$$L=\frac{1}{y}+\frac{1}{0.225\delta} \tag{4}$$

To simulate transition behaviors from the viscous sublayer to the log-law region on the airfoil surface, the Van Driest-type damping function is added into the dissipation rate formulas as in the work.[27] The near-wall transition behaviors are deduced by the already mentioned implementations with the dissipation rate ϵ as

$$\epsilon=\frac{2.5u_\tau^3}{y}\left[1-\exp\left(-\frac{.04\rho u_\tau y}{\mu_l}\right)\right] \tag{5}$$

where u_τ is the friction velocity.

Numerical Methods

The governing equations are integrated by a dual time-stepping procedure and discretized in the finite volume formulation in the present study. Following the work,[28] a second-order accurate, three-point backward differencing is implemented for the physical time discretization, and the second-order explicit Runge–Kutta scheme for the pseudotime evolution of solutions between the physical times. A high-order accurate flux extrapolation[29] is used in the inviscid flux discretization. Central differencing is used for the evaluation of the viscous fluxes. Some details of the preceding procedures are respectively described in the following.

Time Integration

Introduction of a fictitious (pseudo) time τ in Eq. (1) leads to the following set of equations:

$$\frac{\partial Q}{\partial \tau}=-\frac{\partial Q}{\partial t}-\frac{\partial F}{\partial x}-\frac{\partial G}{\partial y}+\left(\frac{\partial F_v}{\partial x}+\frac{\partial G_v}{\partial y}\right)=-\frac{\partial Q}{\partial t}-\mathrm{Res}(Q) \tag{6}$$

The evolution of the residual $[\mathrm{Res}(Q)+\partial Q/\partial t]$ at cell (i, j) in each pseudotime step is calculated by a two-stage, explicit, Runge–Kutta time-marching scheme. In the predictor step

$$\bar{Q}=Q_p-\Delta\tau\left[\mathrm{Res}(Q_p)+\frac{\partial Q_p}{\partial t}\right] \tag{7}$$

$$=Q_p-\Delta\tau \mathrm{Res}^*(Q_p) \tag{8}$$

where the physical-time derivative is approximated by a second-order accurate backward Euler formula:

$$\frac{\partial Q_p}{\partial t}=\frac{3Q_p-4Q^n+Q^{n-1}}{2\Delta t} \tag{9}$$

In the preceding equations $\Delta\tau$ is determined in accordance with the local time-step criteria, whereas Δt is chosen based on the accuracy required for the evolution of unsteady flow simulations; subscript p is the iteration counter in the pseudotime level, and superscript n denotes the physical time level.

Next follows the corrector step

$$Q_{p+1}=Q_p-(\Delta\tau/2)\left[\mathrm{Res}^*(Q_p)+\mathrm{Res}^*(\bar{Q})\right] \tag{10}$$

The iteration in the pseudotime level is accomplished when $\|Q_{p+1}-Q_p\|\leq$ preset tolerance and the solution is set to the next physical time level:

$$Q^{n+1}=Q_{p+1} \tag{11}$$

To reduce computational cost, a local time-stepping and an implicit residual smoothing procedure are employed to speed up the convergence in the pseudotime level. The details about implementation of these techniques can be found in the study.[28]

Numerical Flux

In this section we describe the AUSMD scheme along one of the coordinate lines. First, we define the interface mass flux as

$$(\rho u)_{\frac{1}{2}}=\rho_L u_L^+ + \rho_R u_R^- \tag{12}$$

where subscripts L and R denote the left and right states with respect to the interface. The essential departure of the preceding equation from the AUSM$^+$ scheme lies in the the velocity splittings. Here (u_L^+, u_R^-) are defined as

$$u_L^+=\alpha_L\left[\frac{(u+a)^2}{4a}-\frac{u+|u|}{2}\right]_L+(1-\alpha_L)\frac{u_L+|u_L|}{2} \tag{13}$$

$$u_R^-=\alpha_R\left[-\frac{(u-a)^2}{4a}-\frac{u-|u|}{2}\right]_R+(1-\alpha_R)\frac{u_R-|u_R|}{2} \tag{14}$$

where a is the common (interface) speed of sound

$$a_{\frac{1}{2}}=\tfrac{1}{2}(a_R+a_L) \tag{15}$$

The parameters α_L and α_R are determined such that the numerical dissipation for the contact discontinuity vanishes. Several choices are possible. The original formula by Wada and Liou[25] is based on the ratio of pressure to density:

$$\alpha_L = \frac{2(p/\rho)_L}{(p/\rho)_L + (p/\rho)_R}, \qquad \alpha_R = \frac{2(p/\rho)_R}{(p/\rho)_L + (p/\rho)_R} \tag{16}$$

In this paper we use a new weighting function based only on density[24]:

$$\alpha_L = \frac{2\rho_R}{\rho_L + \rho_R}, \qquad \alpha_R = \frac{2\rho_L}{\rho_L + \rho_R} \tag{17}$$

This choice has the benefit of being free from multidimensional shock instability or the so-called carbuncle phenomenon.

As for the pressure flux, it is defined in the same way as in AUSM$^+$. Let

$$M_L = u_L / a_{\frac{1}{2}}, \qquad M_R = u_R / a_{\frac{1}{2}} \tag{18}$$

Then the split pressures are given by

$$p^{\pm} = \begin{cases} p(M \pm 1)^2 (2 \mp M)/4, & \text{if} \quad |M| > 1 \\ p(M \pm |M|)/2M, & \text{otherwise} \end{cases} \tag{19}$$

The interface pressure is simply the sum of the respective left and right components

$$P_{\frac{1}{2}} = p_L^+ + p_R^- \tag{20}$$

The interface flux for the AUSMD scheme now takes the form

$$F_{\frac{1}{2}} = \tfrac{1}{2}(\rho u)_{\frac{1}{2}}(\Phi_L + \Phi_R) - \tfrac{1}{2}\left|(\rho u)_{\frac{1}{2}}\right|(\Phi_R - \Phi_L) + P_{\frac{1}{2}} \tag{21}$$

where $\Phi = [1, u, v, H]$ and $P = [0, p, 0, 0]$.

To enhance the numerical accuracy, a second-order-accurate flux extrapolation[29] is used. The interface flux now is expressed as a central scheme with a second-order accurate addition from the upwind scheme:

$$F_{i+\frac{1}{2}} = \tfrac{1}{2}(F_i + F_{i+1}) - \tfrac{1}{2}\left(F_{i+\frac{3}{2}} - 2F_{i+\frac{1}{2}} + F_{i-\frac{1}{2}}\right) \tag{22}$$

where the subscripts i and $i + 1$ refer to the cell-center values and the half indices denote the numerical fluxes given earlier in Eq. (21). For the problems in this study, there is no need for introducing a limiter function because the flow either remains subsonic or only has mild supersonic pockets. Whereas the gradient is high in the boundary layer, the profiles are smooth, and lowering the numerical accuracy by introducing limiter functions is undesirable.

Results and Discussion

Numerical Validation

Before proceeding to perform the dynamic-stall simulation, numerical validation of the AUSMD scheme was conducted. Calculations were made for the flowfield around a NACA 0012 airfoil with various angles of attack, including those beyond the static stall. The parameters for the first test case[30] are a Mach number of 0.15 and a Reynolds number of 1.8×10^6 on a 279×64 C-type grid. The minimum spacing near the surface is specified to be 0.00001 of the chord length, and all outer boundaries are located at 20 chord lengths away from the body. In Fig. 1 the computed results by the AUSMD scheme are compared against the experimental data. The predicted lift coefficients agree well with the measured data for cases where the airfoil flow is either stalled or mildly separated. Besides, the predicted lift coefficient vs angle of attack nearly coincides with the data, even in the post-stalled range. Similar data in the comparable range of parameters were taken by several other authors, and their results are basically scattered about the same curve.

To further the validation test, we consider the numerical accuracy of surface pressure simulation with different NACA airfoils. In Fig. 2 we first show the comparison between the calculated and measure pressure coefficients. The test case involves a steady-state NACA 0012 airfoil at a freestream Mach number of 0.3 and a Reynolds number of 3×10^6 like the conditions[31] with an angle of attack of 3.28 deg. The result of AUSMD is seen to be in good agreement with the experimental data. Subsequently, two separated flow cases[21] of the NACA 0015 airfoil with the high angle of attack are selected to verify the computations. The experimental data and the computed solution are depicted in Fig. 3 for the comparison. In both the mildly and strongly separated cases at the angles of attack of 13 and 17 deg, respectively, the calculated surface pressure distributions are in good agreement with the data, with the pressure side predicted more accurately than the suction side.

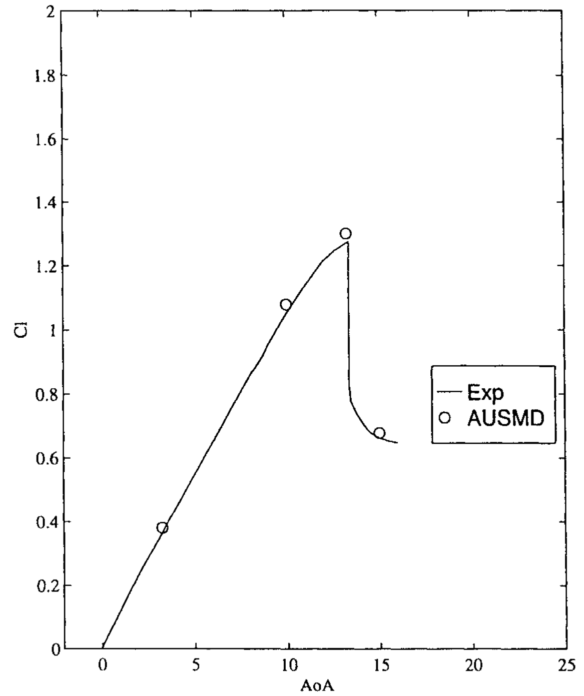

Fig. 1 Lift coefficient C_L vs angle of attack for flows over NACA 0012 airfoils, with $M = 0.15$, by the AUSMD.

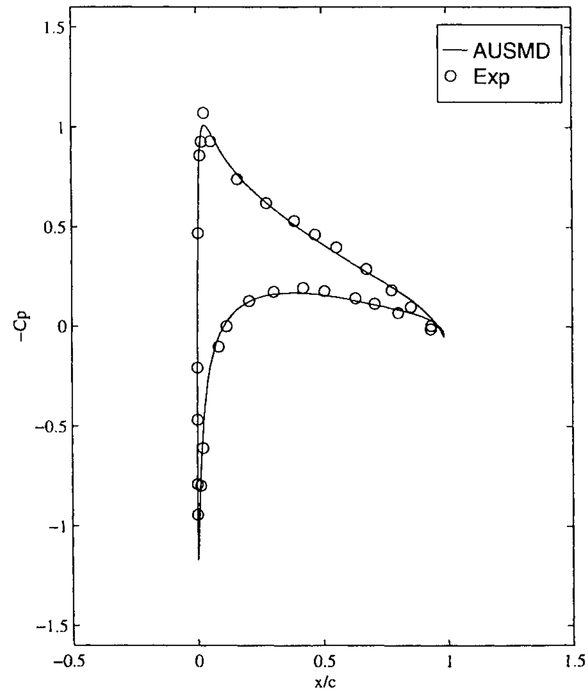

Fig. 2 Pressure coefficient distributions over an NACA 0012 airfoil, with $M = 0.3$ and $\alpha = 3.28$ deg, by the AUSMD.

During the study, we found that the pressure-weighting function appearing in velocity splittings [Eq. (16)] resulted in numerical instability in the vortex-dominated flow. However, using the new weighting function [Eq. (17)] based solely on the density ratio yielded a stable solution for the problem considered. The results for

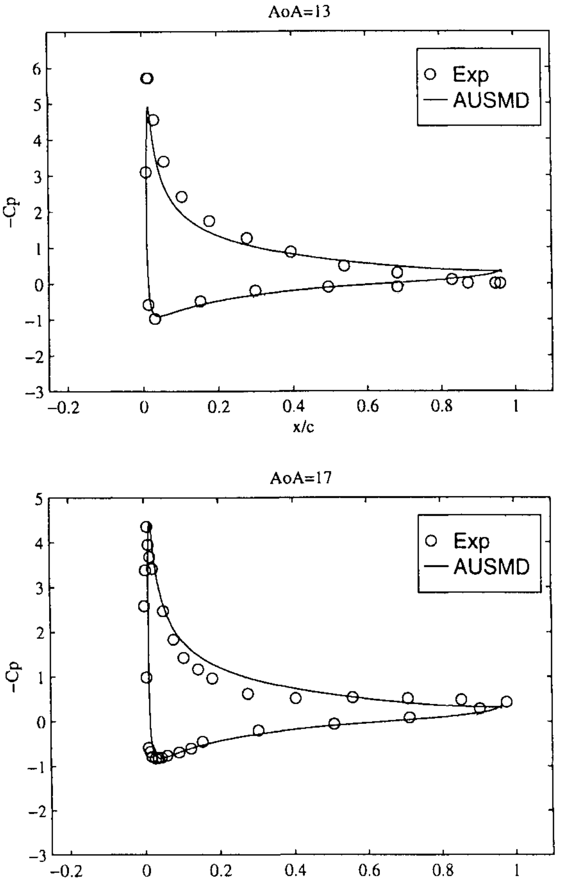

Fig. 3 Pressure coefficient distributions over an NACA 0015 airfoil, $M = 0.29$, $Re = 1.95 \times 10^6$ with $\alpha = 13$ and 17 deg, by the AUSMD.

the just-discussed validation tests were virtually identical. Consequently, the AUSMD with density-weighted velocity splitting was judged to be suitable for the further simulation of the dynamic stall problem.

Dynamic Stall

One light and one deep dynamic-stall case in the experiment of McCroskey et al.[10] are used for validating the calculations. The boundary conditions for viscous flow over the dynamic airfoil are similar to those used for the stationary airfoil. The density is determined from the point next to the body surface. The tangential and normal velocities of the moving surface are equal to the surface grid velocities ($u = x_t$, $v = y_t$). The pressure is determined by solving the normal momentum equation. Uniform flow conditions are specified at the far-field boundaries. At the downstream boundary variables are extrapolated from the interior points to the boundary points. To keep the unsteady time accuracy, local time stepping with Courant–Friedrichs–Lewy (CFL) $= 0.3$ is used for the inner iteration, and $\Delta t = 0.001$ is chosen for the physical time discretization. The instantaneous locations of the airfoil surface are obtained from the prescribed surface motion as defined in Eq. (23). The entire mesh is moved with the airfoil surface at each time step of the calculations. In the present study the airfoil is pitching according to the following motion:

$$\theta = \theta_m + \theta_0 \sin(2kt) \tag{23}$$

where $k = \omega C / 2U_\infty$ is the reduced frequency, θ_m is the mean pitching angle of attack, θ_0 is the amplitude of the sinusoidal oscillation, ω is the frequency of oscillation, k is the reduced frequency, C is the chord length of airfoil, and U_∞ is the freestream velocity.

In the light stall case the parameters chosen for the calculations are $M_\infty = 0.3$, $\theta_m = 10$ deg, $\theta_0 = 5$ deg, $k = 0.2$, and the center of pitching is at $0.25C$. The unsteady calculations were started from the steady solutions at the mean pitching angle of attack. The grid was a 249×64 O-type grid, with minimum spacing near the surface specified to be 0.00001 of the chord length and the outer boundary located at 20 chord lengths away from the body. A fine grid was generated by doubling grid points on the airfoil, and its results will be compared with that of the coarse grid.

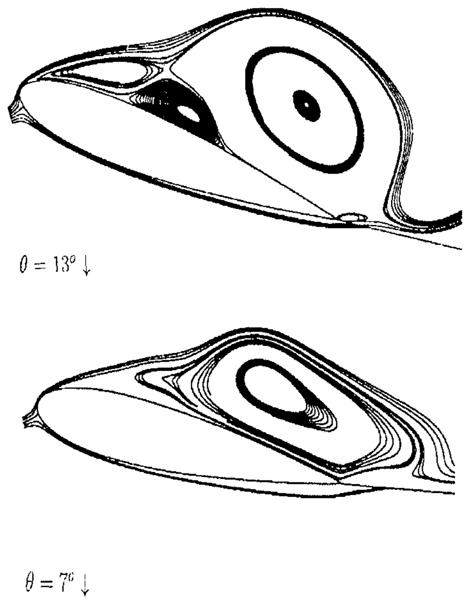

Fig. 4 Particle trace plots in the downstroke of the light stall.

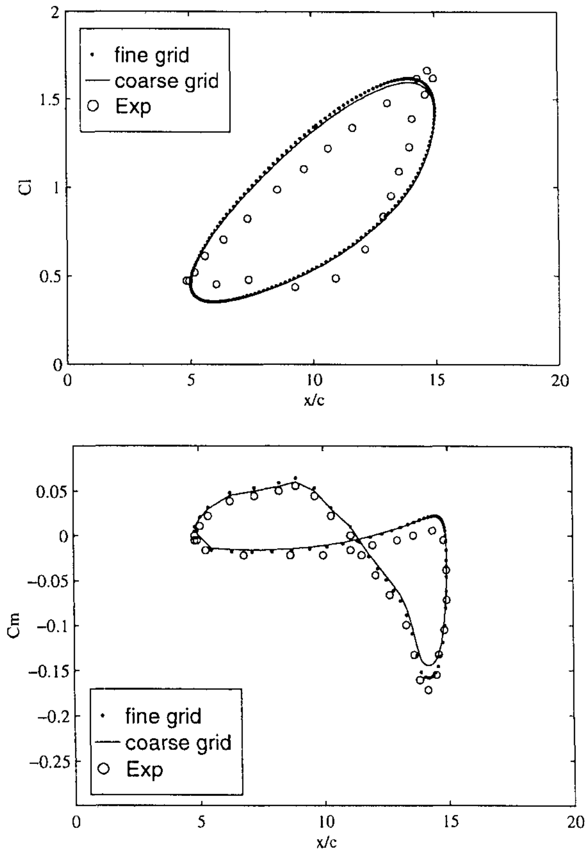

Fig. 5 Lift and moment coefficient hysteresis vs angle of attack of the light-stall case.

First, we present results of the light-stall case on coarse grids. Figures 4 show the particle trace plots of the light dynamic-stall process obtained by computing two cycles of sinusoidal oscillations. In the numerical results recirculation zones are captured on the upper surface as the pitching motion is in the downstroke mode. From unsteady lift and moment coefficient distributions, shown in Fig. 5, the entire event of the light dynamic stall can be seen clearly.

The pitching airfoil passes the static-stall angle during the upstroke motion without the lift loss, which occurs during the static stall. The unsteady lift is increased until the pitching motion reaches an angle of attack of 15 deg. The lift and moment stalls occur near an angle of attack of 15 deg at the beginning of the downstroke modes. The increasing negative moment is stopped near the static stall angle of attack of 13 deg during the downstroke phase. Stall is completed when the pitching down reaches an angle of attack of 10 deg, corresponding to reattachment of the separated boundary layer. As the downstroke stops and upstroke restarts at an angle of attack of 5 deg, the lift and moment coefficients are returned to unstalled values. Numerical prediction of lift and moment coefficient distributions compare well with the measured data. In addition, the predicted unsteady airload hysteresis are demonstrated to be less sensitive to different grids. The current numerical model for the light-stall case is grid independent.

In the deep-stall case the parameters chosen for the calculations are $M_\infty = 0.3$, $\theta(t) = 15 + 10\sin(t/2)$, and again the center of pitching at $0.25C$. Compared to the preceding case, the deep-stall airfoil is located at a larger mean angle and has a larger oscillating amplitude. As before the unsteady calculations were started from steady solutions at the mean pitching angle of attack on a 249 × 64 O-type grid. A fine grid was generated by doubling grid points on the airfoil.

First, we show in Figs. 6 and 7 the particle trace plots of the deep dynamic-stall process, which were obtained by computing two cycles of sinusoidal oscillation on the fine grid. A large separation zone is seen over the entire airfoil near the maximum angle of attack in both the upstroke and downstroke modes. A large vortex is formed at the leading edge, convected along the airfoil surface, and finally shed into the freestream and wake during the nose-down pitching motion. From the grid-refinement study Fig. 8 shows that the vortex captured on the fine grid is larger than the result on the coarse grid. In Fig. 9, the vortex shedding on the fine grid appears to occur earlier than that on the coarse grid, also as expected yielding more details.

Figure 10 shows the history of lift and moment coefficients vs the angle of attack for the deep-stall case, in which the effect of grid sizes is also included in the comparison against the experiment data. The experimental data show that the static-stall angle is exceeded during the nose-up pitching. The unsteady lift is increased until the pitching motion reaches an angle of attack of about 25 deg. At the beginning of the downstroke, the lift stall starts, and a strong negative pitching moment is induced. As the angle of attack decreases, the unsteady lift is reduced until the dynamic stall completes at an angle of attack of about 13 deg. The boundary layer reattaches near the minimum angle of attack for a short period during the pitching motion. As the angle of attack reaches its minimum, the lift begins

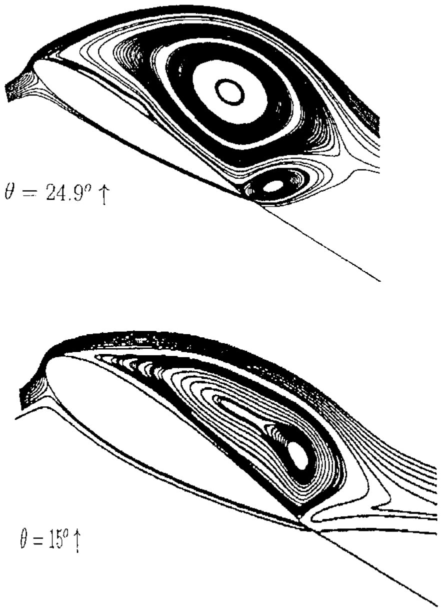

Fig. 6 Particle trace plots in the upstroke of the deep stall.

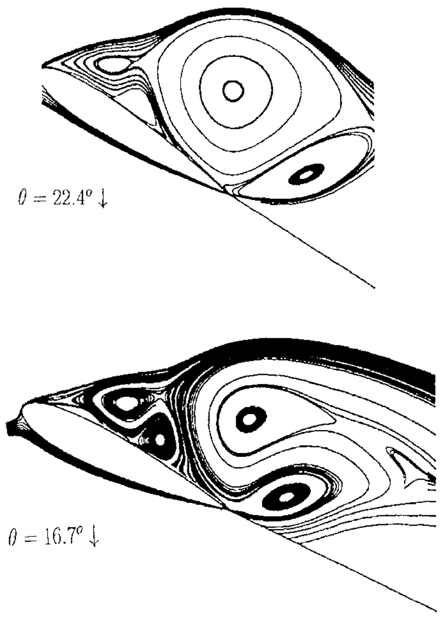

Fig. 7 Particle trace plots in the downstroke of the deep stall.

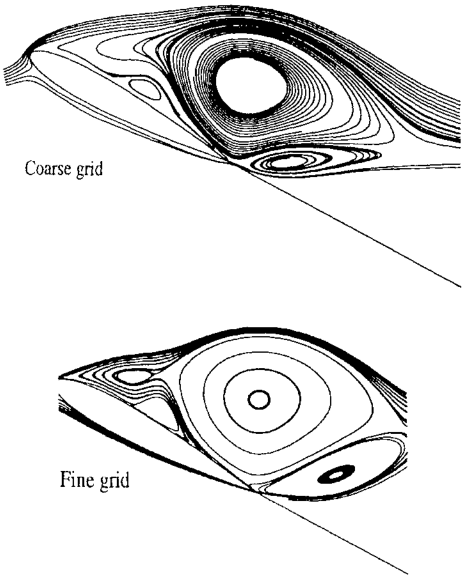

Fig. 8 Particle trace plots at $\theta = 22$ deg ↓ on grid-refinement study.

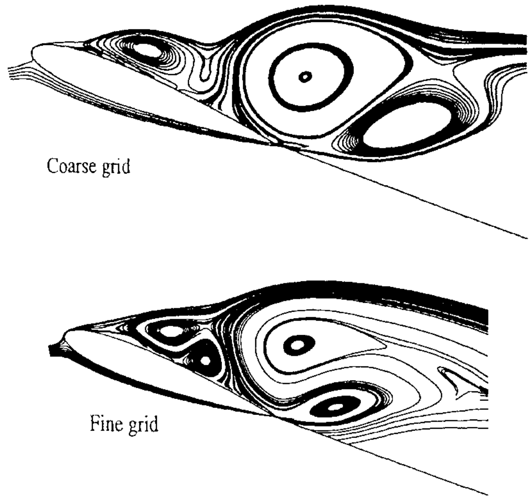

Fig. 9 Particle trace plots at $\theta = 16$ deg ↓ on grid-refinement study.

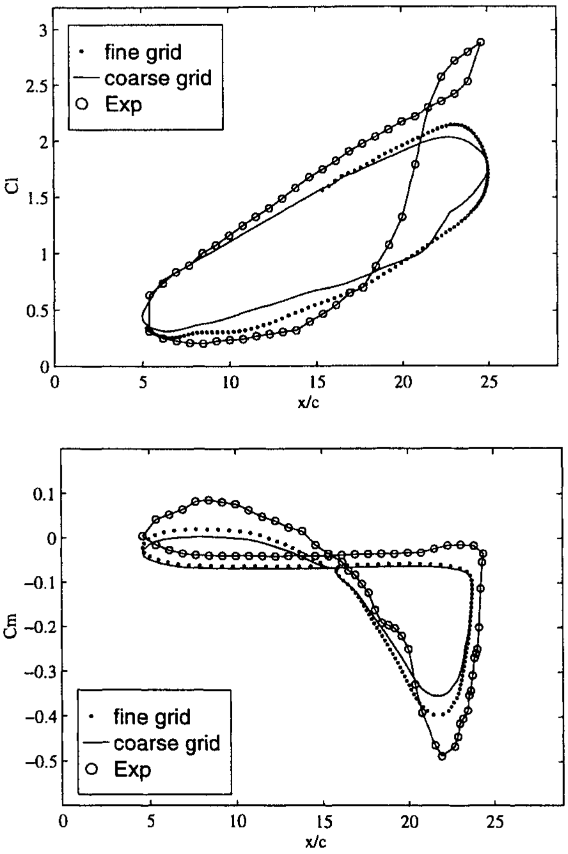

Fig. 10 Lift and moment coefficient hysteresis vs angle of attack of the deep-stall case.

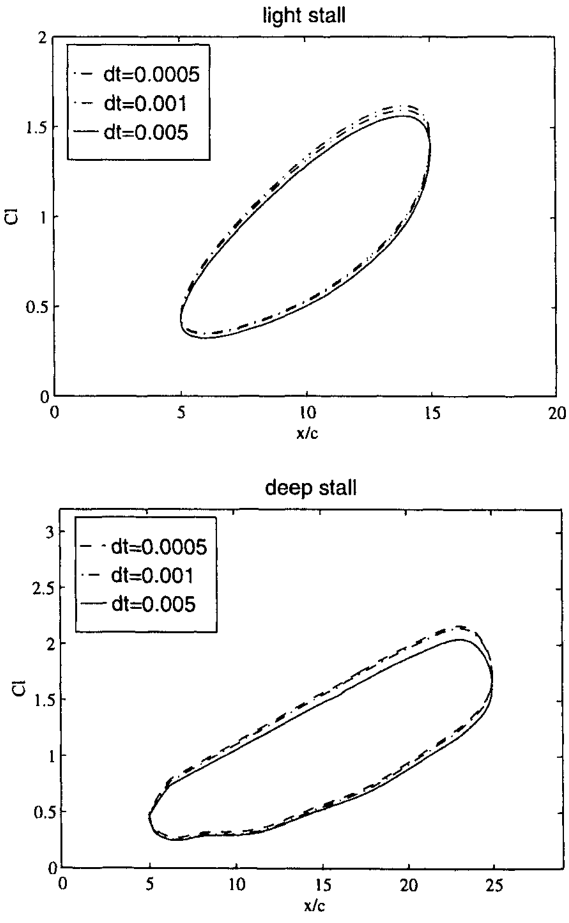

Fig. 11 Influence of the physical time step for lift coefficient hysteresis vs angle of attack.

to increase from its minimum and returns to the unstalled values. In the numerical results a similar tendency in lift and moment coefficients as the measured data is observed. The predicted hysteresis on the fine grid agree slightly better with the experimental data than the coarse grid result. However, the reverse effect in the lift coefficient around the maximum angle of attack of 25 deg in the experimental data is not captured in the numerical results of both grids; also the predicted negative moment coefficients are much smaller than the experimental data. The grid refinement does not show any significant improvement in numerical accuracy of the deep stall simulation.

As a result, we sought to determine whether the physical time step (Δt) influenced the solution. Figure 11 shows the lift coefficient curve for both light-stall and deep-stall cases based on the fine grid with $\Delta t = 0.005, 0.001$, and 0.0005. Again, CFL $= 0.3$ is used in the pseudotime iteration for all of the calculations. The estimated lift hysteresis in both cases are demonstrated to be independent of the physical time step, excepting that the slight under-prediction is seen in the deep-stall case while $\Delta t = 0.005$. The time-step independence for both cases is achieved for $\Delta t \leq 0.001$. However, the deep-stall simulation is not improved by using the smaller physical time step.

Thus, we suspected that the factors turbulence model and especially the transition model and three-dimensional effects might have contributed to the discrepancies. For the current deep dynamic stall case flow separation occurs near the leading edge of the airfoil; the transition of the boundary layer over the airfoil would be critical in determining the flow separation and the subsequent development of the boundary layer. Unfortunately, the current state of the art for predicting flow transition is still in the experimentation stage, namely problem dependent. The situation is even murkier when the flow is unsteady as the flow separates and reattaches cyclically. Also in the systematic evaluation of five turbulence models by Scrinivasan et al.,[21] none of the selected turbulence models have predicted airloads consistently, nor agreed with the experimental data of the deep-stall test cases. A turbulence model with a suitable transition criterion is believed to be a key to solving the dynamic-stall problem. Being unsure of what a transition model would do to the simulation, we did not employ any transition model in the calculation.

Moreover, the study of transition effect on the dynamic stall can be of a significant effort by itself. Nevertheless, we must emphasize the importance of the role that the transition plays in this highly unsteady, separating/reattaching flow. Moreover, the three-dimensional effect, which was not considered in the calculations, is believed to be significant. Because the extent of flow separation and vortex shedding is on the order of the chord length and extends transversely, the effective aspect ratio of the airfoil in the wind tunnel is no longer large. Hence, spanwise, i.e., three-dimensional, effect is not negligible, especially near the maximum angle of attack.

Conclusions

A dual time-stepping method, coupled with the AUSMD scheme, was developed to solve the stationary and dynamic stall problems. The robustness and accuracy are demonstrated in the numerical results. Without artificial damping, coefficients specified as in the widely used central schemes simplified the study of the dynamic-stall calculations. A pseudotime approach was used as an iteration procedure, for which a two-stage Runge–Kutta scheme, local time-stepping, and residual smoothing techniques are implemented, to preserve time accuracy for solving the unsteady equations. A second-order, time-accurate implicit, backward Euler discretization was made at the physical time level, and a high-order-accurate flux extrapolation was used for the spatial discretization. A RNG-based algebraic model was chosen to evaluate effects of turbulence.

The AUSMD scheme with the pressure-weighted velocity splitting, Eq. (16), was found to encounter numerical instability in the vortex-dominated flow. We found that the new weighting function based solely on the density, Eq. (17), was stable for the problem considered, and the calculated steady-state results agree well with the data.

In the numerical results for dynamic stall, significant flow separation and vortex shedding were observed. The unsteady lift was increased until the pitching motion reached near the maximum angle of attack, and a strong negative pitching moment was induced when the dynamic stall was completed. Numerical estimates of the lift and moment coefficients hysteresis were satisfactory in the light-stall case. In the deep-stall case the grid refinement study shows that vortex size was larger and shed earlier on the fine grid than on the coarse grid. However, the peaks in lift and moment coefficients were not predicted by the numerical solutions on both grids. Meanwhile, the predicted airload hystereses are shown to be independent of the physical time step. Therefore, we speculate that the transition in boundary layer and three-dimensional effect might be a key in resolving the discrepancy.

Acknowledgment

The first author wishes to acknowledge the support sponsored by the National Science Council of Taiwan under Contract NSC 87-2213-E-216-024.

References

[1] Carr, L. W., "Dynamic Stall Progress in Analysis and Prediction," AIAA Paper 85-1769, Aug. 1985.

[2] Harris, F. D., and Pruyn, R. R., "Blade Stall–Half Fact, Half Ficition," *Journal of the American Helicopter Society*, Vol. 13, No. 2, 1968, pp. 27–48.

[3] Ham, N. D., and Garelick, M. S., "Dynamic Stall Considerations in Helicopter Rotors," *Journal of the American Helicopter Society*, Vol. 13, No. 2, 1968, pp. 49–55.

[4] Ham, N. D., "Aerodynamic Loading on a Two-Dimensional Airfoil During Dynamic Stall," *AIAA Journal*, Vol. 10, No. 10, 1968, pp. 1927–1934.

[5] Carta, F. O., "Experimental Investigation of the Unsteady Aerodynamic Characteristic of a NACA 0012 Airfoil," Research Rept. M-1283-1, United Aircraft Corp., July 1960.

[6] Liiva, J., and Davenport, F. J., "Dynamic Stall of Airfoil Sections for High-Speed Rotors," *Journal of the American Helicopter Society*, Vol. 14, No. 2, 1969, pp. 26–33.

[7] McCroskey, W. J., and Fisher, R. K., "Detailed Aerodynamic Measurements on a Model Rotor in the Blade Stall Regime," *Journal of the American Helicopter Society*, Vol. 17, No. 1, 1972, pp. 20–30.

[8] McCroskey, W. J., McAlister, K. W., and Carr, L. W., "Dynamic Stall Experiments on Oscillating Airfoils," *AIAA Journal*, Vol. 14, No. 1, 1976, pp. 57–63.

[9] McCroskey, W. J., and Pucci, S. L., "Viscous-Inviscid Interaction on Oscillating Airfoils," AIAA Paper 81-0051, Jan. 1981.

[10] McCroskey, W. J., McAlister, K. W., Carr, L. W., and Pucci, S. L., "An Experimental Study of Dynamic Stall on Advanced Airfoil Sections," NASA TM-84245, July 1982.

[11] McCroskey, W. J., "Unsteady Airfoils," *Annual Review of Fluid Mechanics*, Vol. 14, 1982, pp. 285–311.

[12] McAlister, K. W., Carr, L. W., Pucci, S. L., and McCroskey, W. J., "Dynamic Stall Experiments on the NACA 0012 Airfoil," NASA TP-1100, 1978.

[13] Ono, K., Kuwahara, K., and Oshima, K., "Numerical Analysis of Dynamic Phenomena of an Oscillating Airfoil by the Discrete Vortex Approximation," TR, *Proceedings of the 7th ICNMFD*, Springer–Verlag, New York, 1981.

[14] Ono, K., "Numerical Study of Dynamic Stall Process of a NACA 0012 Airfoil," AIAA Paper 85-0128, Jan. 1985.

[15] Tassa, Y., and Sankar, N., "Dynamic Stall of NACA 0012 Airfoil," AIAA Paper 81-1289, Jan. 1981.

[16] Visbal, M. R., "Evaluation of an Implicit Navier–Stokes Solver for Some Unsteady Separated Flows," AIAA Paper 86-1053, Jan. 1986.

[17] Visbal, M. R., "Effect of Compressibility on Dynamic Stall of a Pitching Airfoil," AIAA Paper 88-0132, Jan. 1988.

[18] Rumsey, C. L., and Anderson, W. K., "Some Numerical and Physical Aspects of Unsteady Navier–Stokes Computations over Airfoils Using Dynamic Meshes," AIAA Paper 88-0329, June 1988.

[19] Visbal, M. R., and Shang, J. S., "Investigation of the Flow Structure Around a Rapidly Pitching Airfoil," *AIAA Journal*, Vol. 30, No. 8, 1992, pp. 911–922.

[20] Visbal, M. R., "Structure of Vortex Breakdown on a Pitching Delta Airfoil," AIAA Paper 93-0434, Jan. 1993.

[21] Scrinivasan, G. R., Ekaterinaris, J. A., and McCroskey, W. J., "Dynamic Stall of an Oscillating Wing, Part 1: Evaluation of Turbulence Models," AIAA Paper 93-3403, June 1993.

[22] Liou, M. S., and Steffen, C. J., "A New Flux Splitting Scheme," *Journal of Computational Physics*, Vol. 107, July 1993, pp. 23–39.

[23] Liou, M. S., "Progress Towards an Improved CFD Method: AUSM+," AIAA Paper 95-1701, June 1995.

[24] Liou, M. S., "Probing Numerical Fluxes: Mass Flux, Positivity, and Entropy-Satisfying Property," AIAA Paper 97-2035, June 1997.

[25] Wada, Y., and Liou, M. S., "A Flux Splitting Scheme with High-Resolution and Robustness for Discontinuities," AIAA Paper 94-0053, Jan. 1994.

[26] Sakya, A. E., Nakamura, Y., and Yasuhara, M., "Evaluation of an RNG-Based Algebraic Turbulence Model," *Computers and Fluids*, Vol. 22, No. 2, 1993, pp. 207–214.

[27] Patel, V. C., Rodi, W., and Scheurer, G., "Turbulence Models for Near-Wall and Low Reynolds Number Flow," *AIAA Journal*, Vol. 23, No. 9, 1985, pp. 1308–1330.

[28] Arnone, A., Liou, M. S., and Povinelli, L. A., "Integration of Navier–Stokes Equations Using Dual Time Stepping and a Multigrid Method," *AIAA Journal*, Vol. 33, No. 6, 1995, pp. 985–990.

[29] Hirsch, C., *Numerical Computation of Internal and External Flows*, Vol. 2, Wiley, New York, 1990, pp. 504–511.

[30] Critzos, C., and Heyson, H. H., "Aerodynamic Characteristics of the NACA 0012 Airfoil Section at Angles of Attack from 0° to 180°," NASA TN-3361, Jan. 1955.

[31] Harris, C., "Two-Dimensional Aerodynamic Characteristic of the NACA 0012 Airfoil in the Langley 8-foot Transonic Pressure Tunnel," NASA TM-81972, 1981.

J. Kallinderis
Associate Editor